ACS Sustainable Chemistry & Engineering

pubs.acs.org/journal/ascecg

Research Article

Enhancement of One-Step Catalytic Dimethyl Ether Production from CO_2 via Selective Enrichment of Brønsted Acid Sites on Alumina with Phosphotungstic Acid

Mert Ozden,[†] N. Semih Altinsoy,[†] Ahsan Jalal, Ayse Dilay Erdali, Orhan Ozcan, Ayse Nilgun Akin, Emrah Ozensoy, and Ahmet K. Avci*

Cite This: *ACS Sustainable Chem. Eng.* 2026, 14, 5650−5663

Read Online

ACCESS | Metrics & More | Article Recommendations | Supporting Information

ABSTRACT: The direct hydrogenation of CO_2 to dimethyl ether (DME) is studied using physically mixed bifunctional catalysts composed of conventional $CuO/ZnO/Al_2O_3$ (CZA, for methanol synthesis) and phosphotungstic acid ($H_3[P(W_3O_{10})_4]\cdot xH_2O$, PTA)-modified γ-Al_2O_3 (for methanol dehydration to DME). A 30 wt % PTA loading and calcination at 500 °C optimizes the Brønsted-to-Lewis acid site ratio and total acid site density, confirmed by NH_3-TPD and in situ FTIR analyses of pyridine adsorption. Structural characterization reveals a disordered PTA overlayer on γ-Al_2O_3 at 500 °C, which transforms into ordered WO_3 and $W_{18}P_2O_{59}$ domains at higher temperatures, leading to decreased Brønsted acidity and lower catalytic performance. Methanol adsorption on the optimized catalyst is examined using in situ FTIR spectroscopy to shed light on the catalytic dehydration of methanol to DME. Methanol dehydration proceeds without the formation of formate intermediates, thus suppressing the generation of side products other than DME, and suggesting a Brønsted acid-mediated associative, direct concerted mechanism. TPD analyses further confirm suppressed methanol dehydrogenation and limited byproduct formation (e.g., formic acid and CO), supporting a direct DME-formation pathway on the Brønsted acid-enriched catalyst. Under optimized reaction conditions (245 °C, 3 MPa, CZA/acid catalyst mass ratio = 1/1), the CZA+PTA/γ-Al_2O_3 catalyst achieves a CO_2 conversion of 21.4%, a DME yield of ∼12%, and a DME productivity of 6.9×10^{-3} kg_{DME} kg_{cat}^{-1} h^{-1} corresponding to more than twice that of the benchmark CZA+γ-Al_2O_3 system. Stability tests over 72 h reveal ∼8% deactivation, which decreases to <3% at 48−72 h, confirming good hydrothermal durability. These results highlight that tuning the surface acidity and structural properties of γ-Al_2O_3 via PTA incorporation, in combination with a conventional CZA catalyst, provides a robust platform for efficient low-temperature CO_2-to-DME conversion.

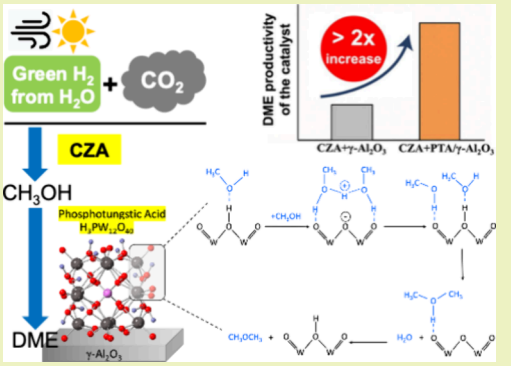

KEYWORDS: *CO_2, hydrogenation, dimethyl ether, phosphotungstic acid, Brønsted acidity, methanol dehydration*

1. INTRODUCTION

The adverse impacts of global warming on the climate and environment have promoted efforts to reduce the carbon dioxide (CO_2) footprint of conventional technologies.[1,2] In this context, the synthesis of sustainable alternative fuels, such as dimethyl ether (DME), using CO_2 as the carbon source has garnered considerable interest.[3,4] DME is an alternative to conventional diesel, offering soot-free, efficient combustion with reduced CO, NO_x, and hydrocarbon emissions, and can be blended with liquefied petroleum gas (LPG) for domestic use.[5] Additionally, DME is a potential hydrogen carrier due to its favorable liquefaction and storage properties, and it serves as a platform chemical for the synthesis of olefins and aromatics.[6]

Traditional DME synthesis involves a two-step process in which methanol is first produced from synthesis gas (syngas: $CO+CO_2+H_2$) on a Cu-based catalyst and then dehydrated to DME in a second reactor packed with a solid acid catalyst (typically γ-Al_2O_3).[7] However, this method is limited by the thermodynamic constraints of methanol production, which require high pressures and recycling to achieve acceptable reactant conversions.[8] This limitation is addressed by combining the methanol synthesis and methanol dehydration reactions in a single reactor, using either the pertinent catalysts, typically in a physically mixed form, or a hybrid catalyst decorated with multiple active sites associated with both reactions. The so-called one-step route promotes the immediate conversion of synthesized methanol to DME and reduces the impact of thermodynamic constraints on methanol

Received: December 10, 2025
Revised: March 3, 2026
Accepted: March 4, 2026
Published: March 12, 2026

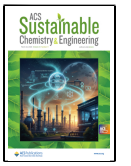

https://doi.org/10.1021/acssuschemeng.5c13468
ACS Sustainable Chem. Eng. 2026, 14, 5650−5663

formation.[7,9] Such an intensification scheme promotes CO_x conversion and DME synthesis in a single reactor, with capital and operating costs lower than those of the conventional two-step process.[10]

Using captured CO_2 as the carbon source reduces the carbon footprint of DME production related to syngas production. This approach promotes a circular carbon economy by balancing the CO_2 emitted from DME fuel combustion with the CO_2 used in DME production, thereby eliminating net positive carbon release to the atmosphere.[11] The realization of this benefit also depends on producing green H_2 by electrolyzing water with renewable energy (i.e., solar or wind), which is expected to become economically feasible in the near future.[12] The combination of the following reactions can describe the one-step synthesis of DME from CO_2 and H_2:

$$CO_2 + H_2 \rightleftarrows CO + H_2O \qquad \Delta H^\circ = 41.0\ \text{kJ mol}^{-1} \tag{1}$$

$$CO + 2H_2 \rightleftarrows CH_3OH \qquad \Delta H^\circ = -90.4\ \text{kJ mol}^{-1} \tag{2}$$

$$2CH_3OH \rightleftarrows CH_3OCH_3 + H_2O \qquad \Delta H^\circ = -23.0\ \text{kJ mol}^{-1} \tag{3}$$

$$CO_2 + 3H_2 \rightleftarrows CH_3OH + H_2O \qquad \Delta H^\circ = -49.4\ \text{kJ mol}^{-1} \tag{4}$$

Reaction 1, the reverse water−gas shift (RWGS), and CO hydrogenation (reaction 2) are typically run on a Cu-based catalyst. The in situ synthesized methanol is then dehydrated to DME via reaction 3 using an acidic catalyst.[9] Previous studies on unpromoted CZA or promoted catalysts such as CuO-ZnO-ZrO_2 (CZZ) physically mixed with acidic catalysts such as zeolites, PTA/MCM-41, and γ-Al_2O_3 point out 15−46% CO_2 conversion and 15−82% DME selectivity depending on temperature (240−270 °C), pressure (3−5 MPa), gas hourly space velocity (GHSV) (2.5×10^2−4×10^4 NL kg_{cat}^{-1} h^{-1}), and H_2/CO_2 feed ratio (3−5).[9,13−16] In contrast to syngas-to-DME conversion, CO_2 hydrogenation leads to higher H_2O formation, which thermodynamically limits DME production via reaction 3 and causes activity loss due to hydrothermal sintering and competitive adsorption with methanol on the acidic sites of the dehydration catalyst.[6,17] In addition to the in situ withdrawal of H_2O from the reactive mixture via steam-selective membranes[18−22] and adsorbents,[23−26] reducing H_2O adsorption on the acidic catalyst is considered a strategy to mitigate the adverse impacts of the hydrothermal reaction environment.[27,28] Due to its favorable DME selectivity, γ-Al_2O_3 is widely studied as an acidic catalytic component. However, the Lewis acid sites in γ-Al_2O_3 suffer from high susceptibility to H_2O.[29] H-ZSM-5, another widely investigated methanol dehydration catalyst, involves Brønsted acid sites, which make it less susceptible to hydrothermal conditions.[30−33] Moreover, ferrierite-type zeolites exhibit excellent activity and stability features in reaction 3.[34−36] However, when these materials coexist with Cu-based metallic catalysts for driving one-step CO_2-to-DME conversion, active site loss can occur due to the exchange of zeolite protons by Cu^{2+} ions.[16,30,37] Bonura et al.[16] reported that the interaction between the metal-oxide phase and the zeolite was the only root cause of activity loss that occurred in the early stages (<10 h) of the CO_2 hydrogenation run at 260 °C, 3 MPa, GHSV = 8800 NL kg_{cat}^{-1} h^{-1}, and $H_2/CO_2/N_2$ = 9/3/1 on CZZ-Zeolite (Sil-1, MFI, Zeolite Y, FER, BEA, MOR) catalyst mixtures. Ren et al.[32] reported a decrease in CO_2 conversion from 25.6 to 21.4% and in DME yield from 17.8 to 11.9% during 100 h time-on-stream (TOS) CO_2 hydrogenation testing over mechanically mixed Cu-ZnO and H-ZSM-5 catalysts at 240 °C, 2.8 MPa, GHSV = 1525 NL kg_{cat}^{-1} h^{-1}, and H_2/CO_2 = 3/1. These findings underscore the importance of acid catalysts that enable stable DME production.

Supported heteropolyacid (HPA) catalysts exhibit superior activity and stability in reaction 3. SiO_2 and TiO_2-supported silicotungstic acid (HSiW) catalysts can deliver >80% methanol conversion (i.e., >90% of the pertinent thermodynamic limit) and a DME production rate of 40−50 mmol DME g_{cat}^{-1} h^{-1} at 180 °C and 1 bar.[38] Moreover, the HSiW/TiO_2 catalyst can offer stable (80 h) methanol conversions of 85−90% (i.e., close to the thermodynamic methanol conversion limit of 91%) at 210 °C and 20 bar.[38] Similarly, incorporation of phosphotungstic acid (PTA) into γ-Al_2O_3 increases Brønsted acidity, which promotes resistance to H_2O-induced deactivation during the dehydration of methanol and ethanol.[27,28] The use of mechanically mixed CZA+60%PTA/MCM-41 catalysts with a mass ratio of 4/1 (CZA/PTA/MCM-41) at H_2/CO_2 = 3/1, 250 °C, 45 bar and GHSV of 4×10^4 mL_{CO2} g_{cat}^{-1} h^{-1} gives 8.9% CO_2 conversion and 23.1% DME selectivity without any remarkable activity loss in 120 h TOS testing of one-step CO_2 hydrogenation to DME.[39] While these findings clearly highlight the benefits and prospects of using HPA catalysts for acidic catalytic function in the direct conversion of CO_2 to DME, a detailed molecular-level understanding of these complex catalytic systems has yet to be established.

In this study, we aim to investigate the one-step CO_2-to-DME conversion using a conventional CZA catalyst for methanol synthesis from CO_2, which is physically mixed with acidic γ-Al_2O_3 or PTA/γ-Al_2O_3 for methanol dehydration to DME. The effects of CZA-to-solid acid catalyst mass ratio, reaction temperature, and pressure on CO_2 conversion and DME yield are systematically studied. To elucidate structure−performance relationships, the catalysts are characterized using Brunauer−Emmett−Teller (BET) specific surface area (SSA) analysis, X-ray diffraction (XRD), ammonia temperature-programmed desorption (NH_3-TPD), H_2-temperature-programmed reduction (H_2-TPR), X-ray photoelectron spectroscopy (XPS), Raman spectroscopy, and in situ Fourier transform infrared (FTIR) spectroscopy. The effects of PTA loading and calcination temperature on acidity and long-term stability are examined. The results clearly show that tuning the surface acidity and structural properties of γ-Al_2O_3 via PTA addition enables Brønsted acid-mediated catalysis, favoring the direct methanol-to-DME pathway and ruling out mechanisms of methanol breakdown into other side products. Moreover, the physical combination of the optimized PTA/γ-Al_2O_3 and conventional CZA catalysts results in robust time-on-stream performance in one-step DME synthesis via CO_2 hydrogenation and significantly outperforms the benchmark CZA+γ-Al_2O_3 case.

2. EXPERIMENTAL SECTION

2.1. Synthesis of the CZA Catalyst

A conventional CZA methanol synthesis catalyst ($CuO/ZnO/Al_2O_3$ = 65/25/10 by mass, nominal) is prepared in-house by ultrasound-assisted one-pot coprecipitation from an aqueous solution of $Cu(NO_3)_2{\cdot}3H_2O$ (Sigma-Aldrich, 99%), $Zn(NO_3)_2{\cdot}6H_2O$ (Sigma-Aldrich, 98%), and $Al(NO_3)_3{\cdot}9H_2O$ (Sigma-Aldrich, 98%) with a

https://doi.org/10.1021/acssuschemeng.5c13468
ACS Sustainable Chem. Eng. 2026, 14, 5650−5663

Na_2CO_3 solution (Sigma-Aldrich, 99.5%) at 70 °C in a 500 mL four-neck flask. First, Cu, Zn, and Al nitrate solution (200 mL, ~0.40 M) is added dropwise using a peristaltic pump (Cole Parmer, Masterflex 7518-00) at a rate of 0.067 $cm^3\ s^{-1}$ to a 200 mL (~0.64 M) Na_2CO_3 (aq.) maintained at 70 °C under continuous ultrasound irradiation at (90 W, SONOPULS HD 3200, 130 mm-diameter Ti horn). Then, the resulting mixture (pH = 8.0−9.0) is first aged for 1 h (20 min with ultrasound + 40 min without ultrasound) at 70 °C, followed by filtration, rinsing with deionized water at room temperature, and treatment in ambient air at 110 °C for 16 h. Next, the samples are cooled to ambient temperature. Finally, the obtained powders are calcined in static air by heating to 300 °C (at a heating rate of 5 °C min^{-1}) and holding at this temperature for 3 h.

2.2. Synthesis of the PTA/γ-Al_2O_3 Catalysts

PTA/γ-Al_2O_3 catalysts are synthesized using the incipient-to-wetness impregnation method with PTA loadings of 10, 20, 30, and 40 wt %. Before impregnation, γ-Al_2O_3 (Alfa Aesar) is ground and sieved to a particle size of 0.3 mm. The required amount of PTA ($H_3[P(W_3O_{10})_4]\cdot xH_2O$, purity: 99.995%, Sigma-Aldrich) is dissolved in deionized water and then impregnated onto γ-Al_2O_3 support material under vacuum. The resulting slurry is dried at 110 °C for 16 h in air and then calcined in a muffle furnace under static air at 500 °C for 3 h. Based on the characterization of the resulting 10−40% PTA-loaded catalysts (Section 3.1), the 30% PTA loading is found to reveal the maximum acidic strength. Optimal calcination conditions are determined by synthesizing the 30 wt %PTA/γ-Al_2O_3 catalyst using additional calcination temperatures of 300, 400, and 600 °C for 3 h and characterizing the resulting samples. Based on the results presented in Section 3.1, 30 wt %PTA/γ-Al_2O_3 calcined at 500 °C is selected as the lead acidic catalyst. The support material, γ-Al_2O_3, is also used as the benchmark acidic catalyst in the current work. Acidic catalysts synthesized in the current work are named in the following manner: *x*PTA/C*y*, where *x* represents the loading (wt %) of PTA impregnation on γ-Al_2O_3, *C* corresponds to calcination, and *y* stands for the calcination temperature (in °C) in air for 3 h.

2.3. Catalytic Activity Experiments

Catalytic activity experiments are conducted in an experimental system that is capable of precise control of gas flow, pressure, and catalyst temperature. Before each catalytic performance experiment, 1 g of CZA catalyst is mechanically mixed with the acidic catalyst (30PTA/C500 or γ-Al_2O_3) whose amount is determined to achieve the desired catalyst mass ratio in the physical mixture. Mechanical (physical) mixing of the catalysts is preferred over their sequential placement in the reactor due to the superior performance of the former configuration, as discussed elsewhere.[24,40,41] The catalyst mixture is packed into a downflow 1.27×10^{-2} m (inner diameter) stainless-steel reactor tube, and its vertical location is fixed by sandwiching it between the quartz wool plugs. The packed reactor tube is inserted into a Thermcraft XST vertical split-tube furnace and connected to the reaction system by Swagelok fittings. Flow rates of the gases (N_2, CO_2, H_2, Ar, and He, all supplied by Linde GmbH, with a purity of >99.99%) and reactor pressure are regulated by Bronkhorst EL-FLOW mass flow controllers and a Bronkhorst EL-PRESS back pressure regulator (BPR), respectively. The furnace control unit adjusts reaction temperature through a Proportional Integral Derivative (PID) mechanism that receives feedback from a K-type thermocouple inserted into the catalyst bed mixture. Plug flow behavior is ensured, and diffusive transport effects are avoided by providing bed height-to-particle diameter (100 for CZA/acidic catalyst mass ratio = 1/1) and tube-to-particle diameter ratios of 36 that exceed the respective limit values of 50 and 10.[42]

Typical catalytic performance experiments are conducted on the CZA+γ-Al_2O_3 and CZA+30PTA/C500 catalyst mixtures with a CZA/acidic catalyst mass ratio ranging between 0.33 and 1.00 and within a temperature range of 215−265 °C, at 3.0 MPa, and a molar inlet $H_2/CO_2/N_2$ ratio of 3/1/1. The total inlet flow rate is fixed at 25 NmL min^{-1} to maintain a constant CZA catalyst-reactive flow contact time and to deliver the same methanol synthesis function to the acid catalysts. The effect of pressure is also studied within the 1.5−3.0 MPa range by varying the temperature and catalyst composition to obtain the highest productivity, defined as the mass of DME produced per time per mass of catalyst mixture ($kg_{DME}\ kg_{cat}^{-1}\ h^{-1}$). Before each catalytic performance experiment, the pressure in the packed reactor tube is increased to 3.0 MPa under inert N_2 flow to ensure there are no leaks in the reactor, as verified by the absence of a pressure drop exceeding 0.01 MPa over 1 h. The catalyst bed is pretreated under 10 NmL min^{-1} pure H_2 flow at atmospheric pressure and 230 °C for 2 h.[23,24] The pretreatment step is followed by purging with N_2 at 50 NmL min^{-1} and setting the desired reaction temperature and pressure. The reaction is initiated by introducing the reactive flow for 3 h. The product stream is passed through a three-way valve and then transferred to a heated gas line (> 200 °C) to prevent phase change of the condensable species before reaching the first gas chromatograph unit (GC-1, Shimadzu GC-2014). Before data collection, an on/off valve is used to retain the gases in this heated line. The three-way valve is also used to redirect the reactor effluent to a parallel line linked to a cold trap (to remove the condensable components) and the BPR unit. Following a reduction of the gas pressure to 0.10 MPa using a needle valve, the gas sample in the heated line is directed to GC-1 equipped with a thermal conductivity detector (TCD) and a Porapak T-packed column. He is used as the carrier gas to analyze CO_2, DME, H_2O, CH_3OH, and any possible C_1-C_2 hydrocarbons. The exit of the BPR unit is sent to a second GC (GC2, Shimadzu GC-2014) equipped with a Carboxen-1000 packed column and a TCD using Ar as the carrier gas to quantify H_2, N_2, CO, and CO_2. Details regarding the data analysis, calculations, and interpretation of the results associated with the catalytic performance tests are provided in the Supporting Information (SI) Sections 1 and 2, as well as in Figures S1−S3 and Tables S1−S3. N_2 is used as the internal standard to compute the molar flow rates of the species. Six-way valves are utilized for sample collection and injection to both GC units every 0.5 h during the experiments. Considering the induction period of the catalysts, the average of the data collected after the second hour from the onset of the reaction is reported. Catalytic activity is quantified in terms of CO_2 conversion (X_{CO_2}) and yields of DME (Y_{DME}) and other products (CO and methanol, $Y_{CO,\ MeOH}$):

$$X_{CO_2} = \frac{F_{CO_2,in} - F_{CO_2}}{F_{CO_2,in}} \times 100\% \quad (5)$$

$$Y_{DME} = \frac{2F_{DME}}{F_{CO_2,in}} \times 100\% \quad (6)$$

$$Y_{i(CO,MeOH)} = \frac{F_i}{F_{CO_2,in}} \times 100\% \quad (7)$$

In eqs 5−7, $F_{CO_2,in}$ refers to the inlet molar flow rate of CO_2 and F_i refers to the molar flow rate of species (i = CO_2, CO, MeOH, DME) in the product stream. For each catalytic performance test, the atomic carbon balance (defined as the ratio of the absolute value of the difference between the total moles of carbon atoms at the inlet and the exit to the total moles of carbon at the inlet) is calculated as described in SI Section 1. Closure of the carbon balance to < 5% allows meaningful comparisons among experiments and can be used as evidence to rule out the presence of significant amounts of surface carbon species and C_1-C_2 hydrocarbons. Reproducibility of the results is ensured by a < 1% difference between the outcomes of independent identical experiments run under identical conditions. The method of calculating X_{CO_2} from the GC analysis is provided in SI Section 2.

The CZA catalyst prepared according to the protocol given in Section 2.1 is used as the standard Cu-containing catalyst in the present work. The validity of the synthesis protocol is controlled by comparing the synthesized CZA catalyst with a well-known commercial benchmark catalyst (HiFuel R120, Johnson Matthey) having the same nominal composition. Comparative activity tests, presented and discussed in the Supporting Information (SI) Section 3, show that coupling of the synthesized and benchmark CZA

https://doi.org/10.1021/acssuschemeng.5c13468
ACS Sustainable Chem. Eng. 2026, 14, 5650−5663

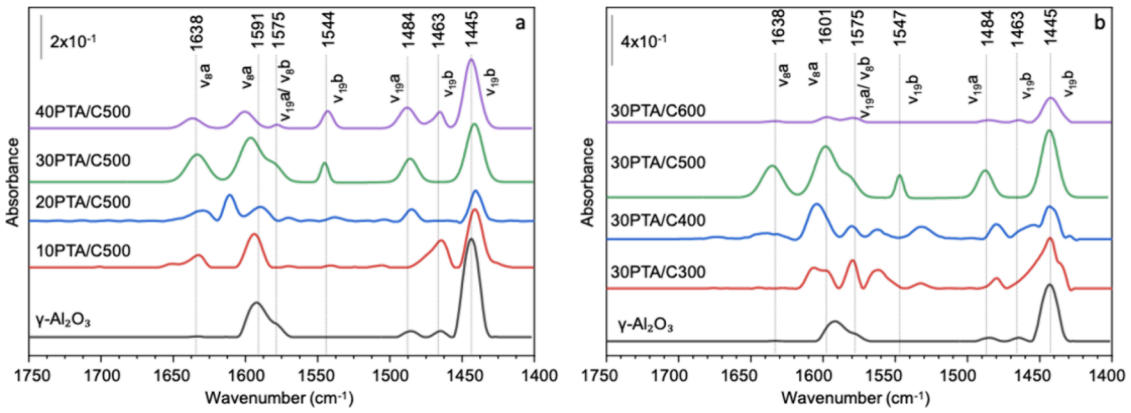

Figure 1. In situ FTIR spectra for the pyridine adsorption on PTA/γ-Al_2O_3 catalysts at 50 °C, followed by evacuation at 100 °C with (a) PTA loadings of 10−40 wt %, all calcined at 500 °C, and (b) PTA loading of 30 wt %, calcined at 300−600 °C. Corresponding data for the γ-Al_2O_3 benchmark catalyst are also shown in both panels.

catalysts with the same solid acid catalyst (30% PTA/γ-Al_2O_3) under identical reaction conditions gives almost the same CO_2 conversion and DME yield. Values of these metrics at thermodynamic equilibrium are computed via the Gibbs free energy minimization technique using ChemCAD software (v. 8.1) as functions of temperature and pressure. These values are also verified by the results of the numerical solutions of the equilibria of reactions 1−4, whose details are reported elsewhere.[22] SI Section 3 also includes the XRD and H_2-TPR analyses of the synthesized CZA catalyst.

3. RESULTS AND DISCUSSION

3.1. Catalyst Characterization

The synthesized PTA/γ-Al_2O_3 catalysts and reference γ-Al_2O_3 are characterized by the BET method for SSA analysis, XRD, Raman spectroscopy, in situ FTIR spectroscopy, NH_3-TPD, H_2-TPR, and XPS. Associated experimental details are provided in SI Section 4. The SSA of bare γ-Al_2O_3 is 269 m^2 g^{-1} and decreases progressively to 242, 169, 149, and 132 m^2 g^{-1} at PTA loadings of 10, 20, 30, and 40 wt %, respectively (Figure S6).

3.1.1. Nature of the Surface Acid Sites: Pyridine Adsorption via In Situ FTIR Spectroscopy. The relative strengths of the surface Brønsted and Lewis acidity of supported HPAs may dictate their catalytic performance in acid-catalyzed reactions, particularly those involving water-rich environments such as CO_2 hydrogenation to DME.[43,44] In situ FTIR spectra obtained after pyridine adsorption on 10−40PTA/C500 and the 30PTA/C300−600 catalysts are presented in Figure 1a and Figure1b, respectively.

These in situ FTIR spectra revealed characteristic bands at 1544 cm^{-1} (ν_{19}b) and 1638 cm^{-1} (ν_8a) that can be assigned to strong Brønsted acid sites, and 1445 cm^{-1} (ν_{19}b) and 1590−1600 cm^{-1} (ν_8a) signals that can be attributed to weak/moderate Lewis acid sites.[45,46] The band at 1484 cm^{-1} (ν_{19}a) is associated with both moderate/strong Brønsted and Lewis acid sites.[46−49] The bands at 1575, 1591, and 1601 cm^{-1} are ascribed to physisorbed pyridine.[47−50] To provide a quantitative evaluation of surface acidity, all pyridine-FTIR spectra are subjected to peak fitting and deconvolution. Using the integrated band areas together with the corresponding molar extinction coefficients (ϵ^B = 1.67 and ϵ^L = 2.22 cm μmol^{-1}), the individual concentrations of Brønsted and Lewis acid sites are quantitatively determined. The resulting values, together with the Brønsted-to-Lewis (B/L) ratios, are summarized in Table 1.

Table 1. Quantification and Characteristics of the Acid Sites of the 30PTA/C300−600 Catalysts Determined from NH_3-TPD and In Situ FTIR Spectroscopic Experiments

catalyst name	integrated NH_3 desorption signal ($\times 10^5$, a.u.) (NH_3-TPD)	catalyst mass (g)	Brønsted-to-Lewis acid site ratio (C_B/C_L) (pyridine adsorption via in situ FTIR)	total moles of acid sites per catalyst mass ($mmol_{NH3}$ g^{-1}) (NH_3-TPD)
30PTA/300	4.1	0.205	0.28	0.5
30PTA/400	4.4	0.229	0.64	0.5
30PTA/500	9.9	0.221	0.69	1.0
30PTA/600	7.8	0.250	0.15	0.6

This quantitative analysis reveals that both the total acidity and the relative contribution of Brønsted acid sites are maximized for the 30PTA/C500 catalyst, which exhibits the highest B/L ratio among the investigated samples. These results indicate that calcination at 500 °C optimally stabilizes Keggin-type, highly dispersed PTA species on the alumina support. In contrast, calcination at 600 °C leads to a pronounced decrease in Brønsted acidity, as evidenced by the strong attenuation of the 1544 and 1638 cm^{-1} bands and a substantial reduction in the B/L ratio. This behavior is consistent with partial decomposition of the heteropolyacid structure and a shift toward a predominantly Lewis-acidic surface, consistent with the structural changes observed by XRD. The enrichment of strong Brønsted acid sites at intermediate calcination temperatures correlates favorably with the superior catalytic performance of the 30PTA/C500 catalyst in DME synthesis and supports the established requirement for robust Brønsted acidity to enhance CO_2 conversion to DME. This observation is also consistent with the expectation that enrichment in Brønsted acidity is beneficial for improving the catalyst's resistance to steam-induced deactivation.

3.1.2. Quantification of Surface Acid Sites: NH_3-TPD. Surface acidity of the 30PTA/C300−600 catalysts is also further investigated via NH_3-TPD (Figure 2 and Table 1). To minimize the interference of water in the quadrupole mass spectroscopy (QMS) signals during NH_3-TPD experiments, the m/z = 16 channel data are selected and smoothened for clarity to monitor the NH_3 desorption process (for the raw data of the TPD plots presented in Figure 2, see Figure S7). It should also be noted that the currently used QMS does not yield any significant mass spectroscopic fragmentation signal at

https://doi.org/10.1021/acssuschemeng.5c13468
ACS Sustainable Chem. Eng. 2026, 14, 5650−5663

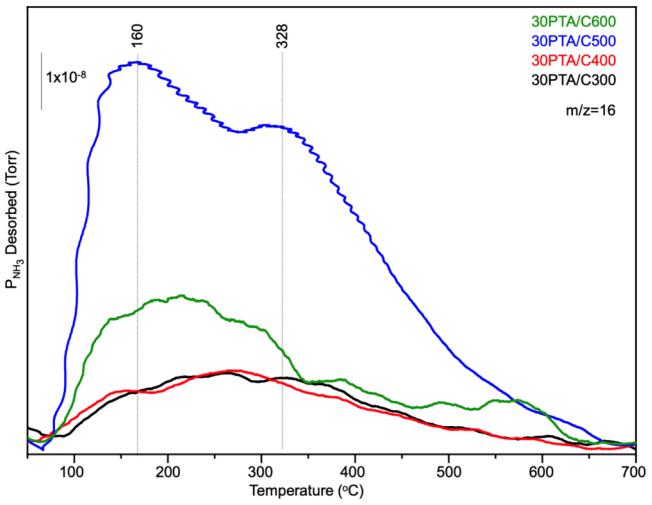

Figure 2. NH_3-TPD profiles for the 30PTA/C300−600 catalyst samples.

m/z = 16 due to H_2O. A typical NH_3-TPD data for the 30PTA/C500 catalyst with multiple desorption channels (m/z = 16, 17, 18) is also presented in Figure S8. The data in Figure 2 reveal desorption features at ca. 160 and 328 °C, which can be attributed to NH_3 desorption from weak and strong acidic surface sites, respectively.[51,52] It is apparent that the NH_3 desorption signal for the 30PTA/C500 catalyst in Figure 2 significantly surpasses that of 30PTA/C300−400−600 catalysts, suggesting the presence of a noticeably greater total number of surface acid sites on 30PTA/C500 than the remaining catalysts (Table 1). The results of NH_3-TPD and in situ FTIR analyses are used to determine the influence of calcination temperature on the total number of acid sites (assuming one NH_3 molecule per acid site) and relative amounts of different types of surface acidic sites (Table 1). The ratios of Brønsted-to-Lewis acid sites reported in Table 1 are calculated from the extinction coefficients of the bands at 1540 cm^{-1} (Brønsted) and 1445 cm^{-1} (Lewis) as explained elsewhere.[53,54] These results clearly show that both the total number of surface acid sites and the Brønsted-to-Lewis acid site ratio are maximized for the 30PTA/C500 catalyst. Moreover, the acidity exhibits a strong dependence on calcination temperature, where calcination at 500 °C enhances Brønsted acidity and yields the highest C_B/C_L ratio (0.69), whereas treatment at 600 °C leads to a pronounced decrease in Brønsted sites and a predominance of Lewis acidity ($C_B/C_L \approx$ 0.15).

3.1.3. Crystal Structure of the PTA Overlayer on γ-Al_2O_3: XRD and Raman Spectroscopy. Structural changes in the crystallinity of the PTA/γ-Al_2O_3 catalysts as a function of PTA loading and calcination temperature are investigated using XRD and Raman spectroscopy. As shown in Figure 3a, XRD patterns of the 10−30PTA/500 catalysts are similar to that of bare γ-Al_2O_3, revealing broad features that are associated with the γ-Al_2O_3 domains, indicating the presence of a highly disordered PTA overlayer structure on γ-Al_2O_3 in agreement with earlier studies.[28,55] The absence of distinct PTA-related XRD signals for 10−30PTA/C500 and 30PTA/C300−400 catalysts suggests that on these catalyst surfaces, small PTA-related sites are presumably well dispersed on alumina and exist in an amorphous form.

In contrast, new diffraction features appear for high PTA loadings and elevated calcination temperatures (i.e., 40PTA/C500 and 30 PTA/C600, Figure 3b). These peaks do not match those of crystalline PTA (ICDD: 00-050-0655), indicating that the PTA structure is no longer preserved under these conditions. Instead, this new set of diffraction features resembled those of WO_3 (ICDD: 00-020-1323) and $W_{18}P_2O_{59}$ (ICDD: 00-041-0371).[56] This finding is also supported by Raman spectroscopy (Figure 4), which shows a new prominent Raman band at 807 cm^{-1} for the 40PTA/C500 and 30PTA/C600 catalysts, corresponding to the presence of crystalline WO_3 domains on these catalysts.[46,57] In addition, Raman signals at 276 and 712 cm^{-1} are also assigned to crystalline WO_3 domains, supporting the degradation and sintering of the well-dispersed and disordered PTA overlayer structure on 40PTA/C500 and 30 PTA/C600 catalysts.[46,54,58] Furthermore, the terminal W═O stretching Raman feature at 980 cm^{-1} is visible in all of the investigated catalysts,[59] and the shoulder at 865 cm^{-1} is attributed to the bending vibration of the W−O_c−W linkages.[54,60] These results indicate that moderate PTA loadings stabilize PTA in the form of a well-

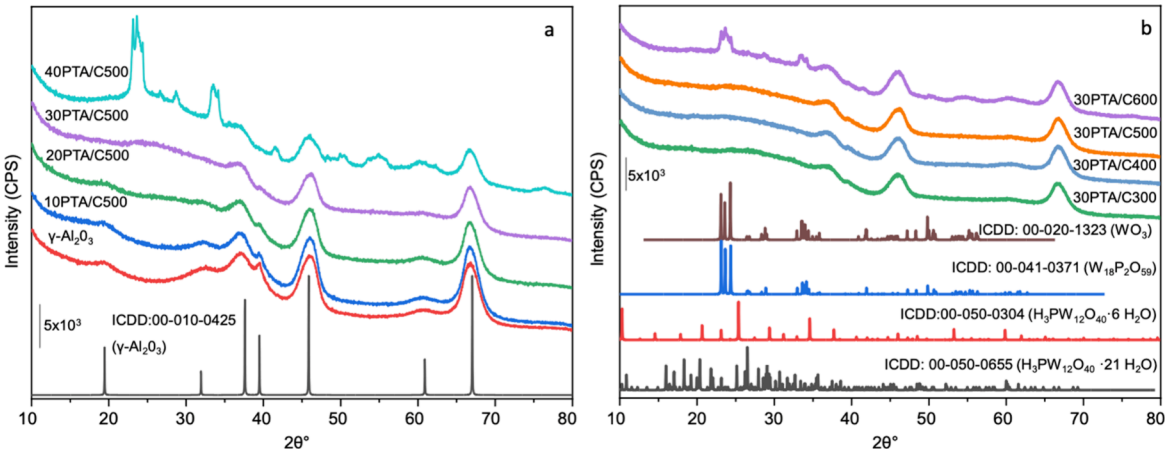

Figure 3. XRD patterns of PTA/γ-Al_2O_3 catalysts: (a) effect of PTA loading (10−40 wt %) at a calcination temperature of 500 °C, showing the preservation of the amorphous nature of PTA on the alumina support at lower loadings, (b) effect of calcination temperature (300−600 °C) for the 30 wt % PTA/γ-Al_2O_3 illustrating phase transformation and the emergence of crystalline phases at higher temperatures, presented along with the corresponding ICDD reference XRD patterns.

https://doi.org/10.1021/acssuschemeng.5c13468
ACS Sustainable Chem. Eng. 2026, 14, 5650−5663

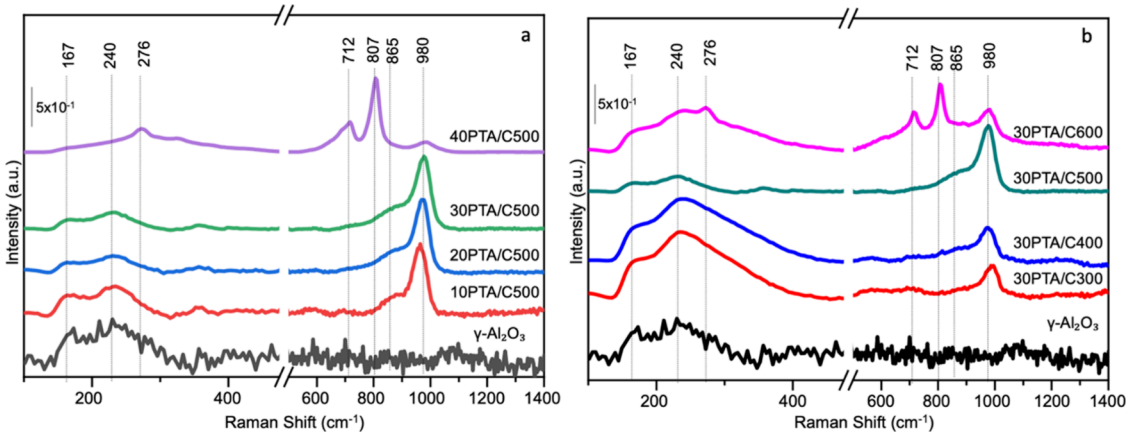

Figure 4. Raman spectra for the catalyst samples involving (a) 10−40PTA/C500 and (b) 30PTA/C300−600. Corresponding data for the γ-Al_2O_3 benchmark catalyst is also shown in both panels.

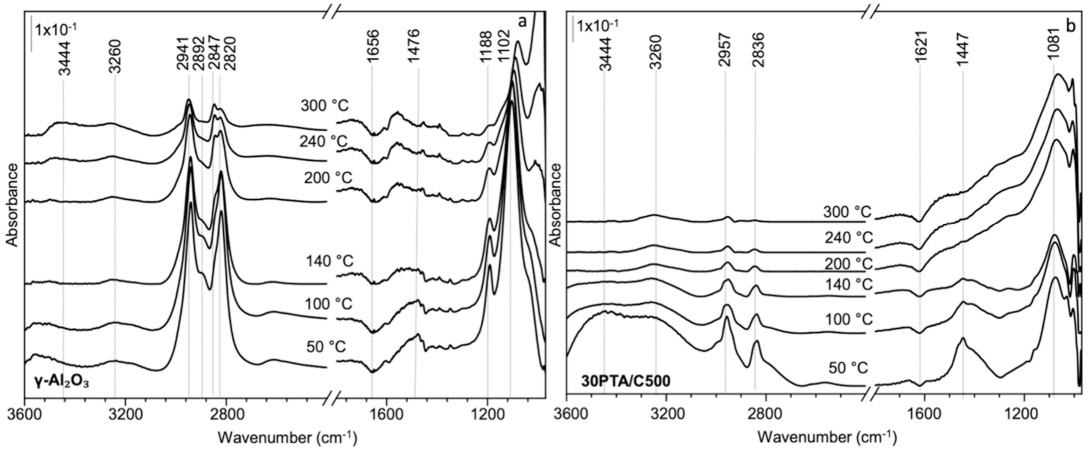

Figure 5. In situ FTIR spectra of methanol adsorption on (a) γ-Al_2O_3 and (b) 30PTA/C500 catalysts, collected during stepwise heating from 50 to 300 °C.

dispersed amorphous overlayer (monotungstate/polytungstate 2D islands or monolayer). In contrast, higher loadings and harsher calcination temperatures promote PTA sintering, decomposition, and the formation of crystalline WO_3 species. This observation is consistent with a previous study on methanol dehydration to DME over WO_x/Al_2O_3 catalysts.[59] In this former work, it is demonstrated that catalytic activity was higher for the disordered monotungstate and polytungstate surface WO_x overlayers on Al_2O_3 below the monolayer WO_x surface coverage. Furthermore, it was shown that the catalytic activity decreased with increasing WO_x surface coverages along with the formation of crystalline WO_3 nanoparticles and large bulk-like WO_3 crystals. Thus, the attenuation in catalytic performance was associated with the loss of strong W−O−Al acidic sites.[59]

3.1.4. Surface Elemental Composition and Oxidation State Analysis by XPS. XPS analysis supports the incorporation of tungsten species on the catalyst surface. As shown in Figure S9 (SI Section 4), XPS-based surface elemental composition analysis confirms the presence of W on the PTA-loaded catalysts. Moreover, W4f spectra (Figure S10a, SI Section 4) reveal that tungsten exists predominantly in the W^{6+} state, as evidenced by the $W4f_{7/2}$ and $W4f_{5/2}$ doublets centered at ca. 35.9 and 38.0 eV, respectively.[61] Variations in W4f peak shapes and shoulders are observed among different catalyst samples. These variations may indicate the presence of minority species comprised of reduced W states; however, their precise and unambiguous identification via spectral deconvolution is challenging due to overlapping signals and the complexity of the W4f signal.[62,63] Similarly, the O1s region shows overlapping contributions from both γ-Al_2O_3 and PTA-related species, making reliable deconvolution imprecise (Figure S10b).

3.1.5. Reducibility of the Catalysts: H_2-TPR. H_2-TPR results of the 30PTA/C300−600 catalysts (Figure S11) show minimal H_2O formation, in line with the reported thermal stability of γ-Al_2O_3 and PTA. γ-Al_2O_3 is not reducible (Figure S11), and PTA remains mostly stable under H_2 up to ∼300 °C.[64−66] The low-temperature H_2O signal is assigned to hydrogen-assisted removal of weakly bound oxygen species from PTA-derived WO_x sites, while the higher-temperature H_2O release (> 300 °C) is attributed to the reduction of bridging W−O−W lattice oxygen, accompanied by partial reduction of W^{6+} to a minority W^{5+} species.[62,65,67]

3.1.6. Types of Adsorbates Generated upon Methanol Adsorption: CH_3OH Adsorption via In Situ FTIR Spectroscopy. Methanol adsorption and thermal evolution of methanol on γ-Al_2O_3 and 30PTA/C500 catalysts are investigated via in situ FTIR spectroscopy to shed light on the catalytic transformations relevant to DME synthesis (Figure 5). Previous reports in the literature[68−71] often proposed that methanol dehydration over acidic catalysts

https://doi.org/10.1021/acssuschemeng.5c13468
ACS Sustainable Chem. Eng. 2026, 14, 5650−5663

Scheme 1. Proposed Concerted Associative Mechanism for Methanol Dehydration to DME over the 30PTA/C500 Catalyst Surface, Adapted from Ref 70.

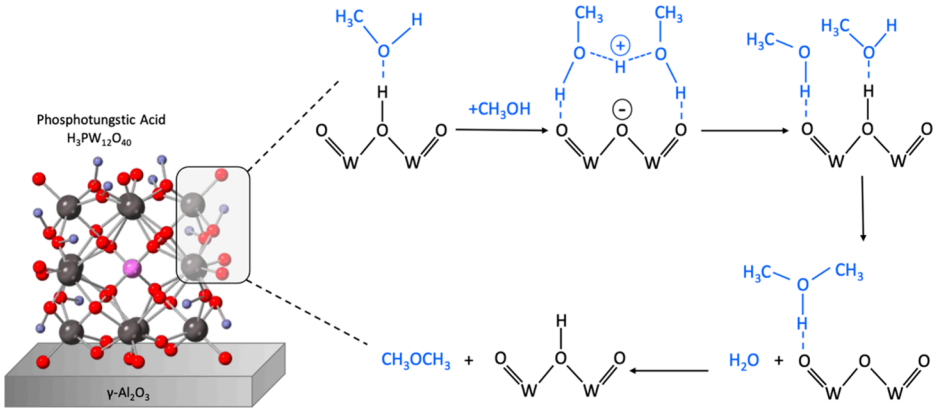

proceeds via multiple pathways depending on the type and strength of acid sites, including dissociative or associative bimolecular routes. In a typical dissociative bimolecular route, methanol may undergo O−H cleavage on a surface Brønsted acid functionality of a bridging oxygen site and result in the formation of an adsorbed methoxy functionality and H_2O via dehydration. Consecutively, this generates methoxy species that may interact with another methanol molecule adsorbed on an adjacent bridging surface oxygen site and leads to $-CH_3$ transfer from methoxy to methanol, producing $CH_3-O(H)-CH_3$ (ads), which desorbs as DME, and regenerates the Brønsted acid functionality on the bridging oxygen site of the surface. On the other hand, in a typical associative route, methanol adsorbed on the Brønsted acid functionality of a surface bridging oxygen site may interact with another adsorbed methanol molecule in proximity on the surface to form a protonated methanol dimer ($H(CH_3)O-(H^+)-O(CH_3)H$), where decomposition of this protonated methanol dimer yields DME and H_2O, while regenerating Brønsted acid site on the surface. In addition to these bimolecular mechanisms, other unimolecular α-elimination pathways have also been proposed, though they are less common.[68−71]

In situ FTIR spectra for methanol adsorption on γ-Al_2O_3 at 50 °C and the thermal evolution of the adsorbates are presented in Figure 5a. A detailed list of IR peak assignments is also provided in Table S5. These results reveal both molecularly adsorbed methanol and dissociatively formed methoxy species on the γ-Al_2O_3 surface, in line with previous reports.[72,73] Broad and relatively weak OH bands at 3444 and 3200 cm^{-1} on the γ-Al_2O_3 surface indicate the presence of a limited extent of hydrogen-bonded adsorbed molecular methanol species on γ-Al_2O_3 interacting with the −OH functionalities of the alumina surface.[72] Dissociative methanol adsorption on γ-Al_2O_3 is observed to occur in two different configurations, namely, bridging methoxy groups, formed on the stronger Lewis acidic sites, and linear methoxy groups, weakly bound on weaker Lewis acid sites. Likely, these bridging methoxy species ($\nu_{asy}(CH_3)$ = 2941 cm^{-1}, $\nu_{sy}(CH_3)$ = 2847 cm^{-1}, $\delta(CH_3)$ = 1458−1454 cm^{-1}, $\nu(CO)$ = 1102 cm^{-1}) are primarily coupled with each other through an associative pathway resulting in the formation a dimer intermediate to yield DME, thus acting as key intermediates in methanol dehydration.[29,73−75] In addition, the weak IR band at 2892 cm^{-1} is assigned to a Fermi resonance of the $\nu_{sy}(CH_3)$ mode.[74,75] Additional features at 1476 and 1458−1454 cm^{-1} ($\delta(CH_3)$) further confirm the coexistence of molecularly adsorbed methanol and different methoxy groups stabilized on Lewis sites (Figure 5a and Figure S12a).[29,75] The negative feature at ∼1656 cm^{-1} (δ(HOH)) is attributed to desorption and substitution of physisorbed water upon methanol adsorption.[76]

Furthermore, in addition to bridging methoxy species, linearly adsorbed methoxy species on γ-Al_2O_3 ($\nu_{sy}(CH_3)$ = 2820 cm^{-1}, ρ(rocking, CH_3), or ν(CO)1188 cm^{-1}) are also visible in Figure 5a at 50 °C.[73] These species are either desorbed as methanol or converted into formate species upon heating.[77,78] The appearance of formate-related bands at 1556 and 1391 cm^{-1} (corresponding to ν_{as}(COO), and ν_s(COO), respectively) on γ-Al_2O_3 (Figure S12a) confirms that methanol undergoes dehydrogenation on γ-Al_2O_3.[74,77,79] In contrast, bridging methoxy species persist even at 300 °C (Figure S13a), underscoring their greater thermal stability and central role in DME formation, whereas linear methoxy species desorb as methanol or transform into formates at elevated temperatures. Note that in the literature, DME formation from methanol is suggested to occur on Lewis acid sites via the dissociative pathway, while the associative mechanism, involving protonation of methanol, is linked to Brønsted acid sites.[51,79]

On 30PTA/C500, methanol adsorption shows features distinct from those on γ-Al_2O_3, due to the significant Brønsted acidity introduced by PTA-related sites. At low temperatures (50−100 °C), strong ν(O−H) hydrogen-bonded bands appear at 3444 and 3260 cm^{-1} (Figure 5b). These bands are more intense than those of γ-Al_2O_3, indicating a stronger interaction between adsorbed methanol species and surface hydroxyl functionalities due to the presence of a greater number of Brønsted acid sites on 30PTA/C500. In parallel, C−H stretching features of adsorbed methanol are observed at 2898, 2957, and 2836 cm^{-1} (Figure 5b and Figure S13b), accompanied by $\delta(CH_3)$ bending at 1466−1447 cm^{-1} and C−O stretching at 1081 cm^{-1}.[80] Upon heating, the methanol-related IR signatures start to attenuate and eventually vanish at 300 °C on 30PTA/C500, while no stable formate signals are observed. The thermal evolution of adsorbed methanol species on 30PTA/C500 is quite different from that on γ-Al_2O_3, where methoxy species persist, and formates accumulate at elevated temperatures (Figure S12b). Based on the current results as well as the former reports in the literature,[68−71] enrichment of the Brønsted acid sites on the 30PTA/C500 catalyst surface coupled with the enhancement in the catalytic activity toward

https://doi.org/10.1021/acssuschemeng.5c13468
ACS Sustainable Chem. Eng. 2026, 14, 5650−5663

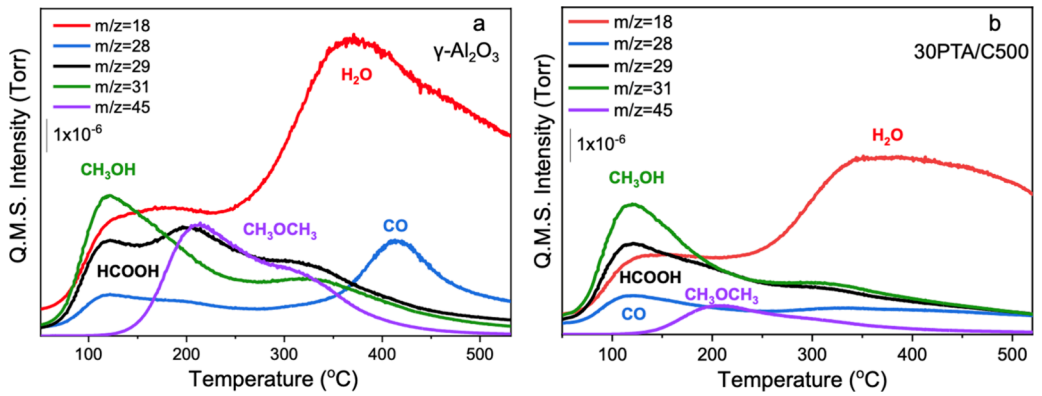

Figure 6. Methanol-TPD profiles on (a) γ-Al_2O_3 and (b) 30PTA/C500 catalysts.

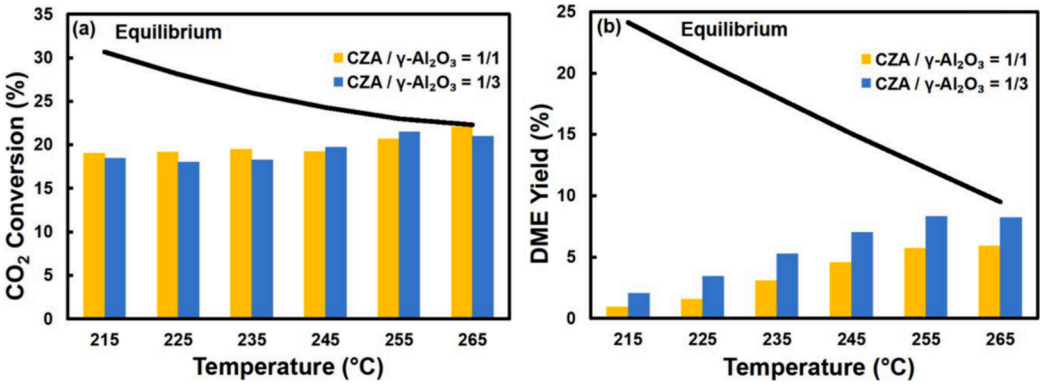

Figure 7. Effect of temperature on the (a) CO_2 conversion and (b) DME yield obtained on the CZA+γ-Al_2O_3 catalyst mixture at CZA/γ-Al_2O_3 mass ratios 1/1 and 1/3.

DME production suggests that a concerted associative reaction mechanism mediated by the surface Brønsted acid sites of the 30PTA/C500 similar to the one given in (eqs 8−12 and Scheme 1) may be operating on the 30PTA/C500 catalyst surface during methanol dehydration to DME:

$$CH_3OH(ads) + H^+(surf) \rightleftarrows CH_3OH\cdots H^+(ads) \quad (8)$$

$$CH_3OH\cdots H^+(ads) + CH_3OH(ads) \rightleftarrows (CH_3OH\cdots H^+\cdots HOCH_3)(ads) \quad (9)$$

$$(CH_3OH\cdots H^+\cdots HOCH_3)(ads) \rightleftarrows CH_3OCH_3\cdots H^+(ads) + H_2O(g) \quad (10)$$

$$CH_3OCH_3\cdots H^+ \rightleftarrows CH_3OCH_3(ads) + H^+(surf) \quad (11)$$

$$CH_3OCH_3(ads) \rightleftarrows CH_3OCH_3(g) \quad (12)$$

In this reaction route, methoxy species are not expected to accumulate on the catalyst surface. The absence of formates favors direct DME formation, which is in line with the current in situ FTIR spectroscopic and catalytic performance data on the 30PTA/C500 catalyst, suggesting that selective enrichment of Brønsted acid sites on the 30PTA/C500 catalyst surface-enhanced DME production on this catalyst as compared to that of other catalysts tested in this study.

3.1.7. Thermal Stability of Surface Species Generated upon Methanol Adsorption: CH_3OH-TPD. Figure 6 shows methanol-TPD measurements on γ-Al_2O_3 and 30PTA/C500 catalysts, obtained under conditions similar to those of the current in situ FTIR measurements. Comparable masses of γ-Al_2O_3 and 30PTA/C500 catalysts are used in the methanol-TPD experiments. However, the relative SSA values of these two catalysts are significantly different (i.e., 269 $m^2\ g^{-1}$ for γ-Al_2O_3 and 149 $m^2\ g^{-1}$ for 30PTA/C500). Figure 6 indicates that molecular methanol desorbs prominently at 120 °C from both catalysts with an additional weaker desorption shoulder at 310−320 °C. While the intensities and line shapes of the molecular methanol desorption signals are rather similar for both catalysts, significantly greater amounts of additional product desorption signals corresponding to HCCOH, CO, H_2O, and DME are observed for γ-Al_2O_3 due to the greater extent of dissociative methanol adsorption on γ-Al_2O_3 as compared to that of 30PTA/C500. Along these lines, Figure 6a and 6b reveals a very intense HCOOH desorption signal for γ-Al_2O_3, which is associated with the greater formate surface coverage as well as the relatively higher thermal stability of formates on γ-Al_2O_3, surpassing that of 30PTA/C500. In good accordance with the current in situ FTIR spectroscopic results for temperature-dependent methanol adsorption (Figure 5), the current methanol-TPD data (Figure 6) also suggest a greater formate surface coverage (evident by the greater total HCOOH desorption signal) and a higher formate thermal stability (apparent by stronger HCOOH desorption at elevated temperatures such as 205 and 310 °C). Furthermore, thermal decomposition of HCOOH on γ-Al_2O_3 probably also occurs at elevated temperatures (>350 °C) in the form of CO(g) and H_2O(g). Note that the water desorption signal at T > 350 °C is also likely to have a contribution from methanol dehydration to form DME as well as dehydroxylation of alumina surface

https://doi.org/10.1021/acssuschemeng.5c13468
ACS Sustainable Chem. Eng. 2026, 14, 5650−5663

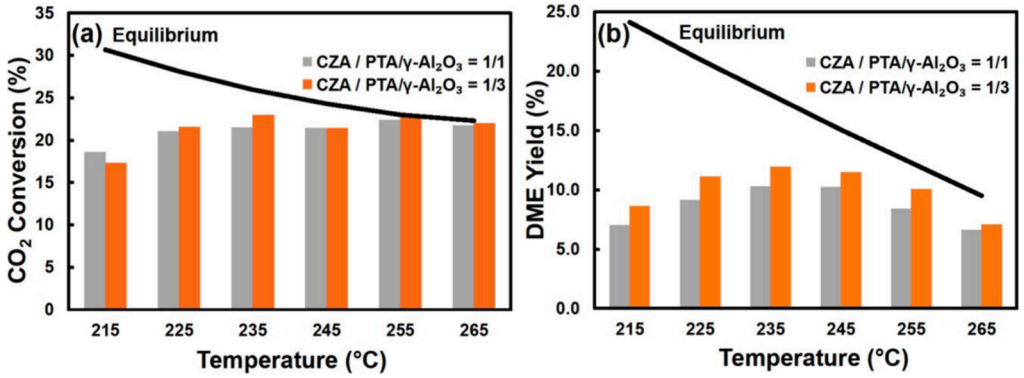

Figure 8. Effect of temperature on the (a) CO_2 conversion and (b) DME yield obtained on the CZA+30PTA/C500 catalyst mixture at CZA/(30PTA/C500) mass ratios 1/1 and 1/3.

Table 2. CO and Methanol Yields Obtained on CZA+γ-Al_2O_3 and CZA+30PTA/C500 Catalysts as Functions of CZA/Acid Catalyst Mass Ratio and Temperature

	CZA/γ-Al_2O_3 = 1/1		CZA/γ-Al_2O_3 = 1/3		CZA/30PTA/C500 = 1/1		CZA/30PTA/C500 = 1/3	
temperature (°C)	Y_{CO} (%)	Y_{MeOH} (%)	Y_{CO} (%)	Y_{MeOH} (%)	Y_{CO} (%)	Y_{MeOH} (%)	Y_{CO} (%)	Y_{MeOH} (%)
215	4.9	10.4	4.4	8.2	5.0	4.1	4.7	3.4
225	5.8	10.9	4.6	8.4	5.3	3.7	4.6	2.4
235	7.1	8.7	5.3	7.3	6.2	3.1	5.3	2.9
245	7.8	8.6	5.6	7.9	7.8	2.5	6.7	2.4
255	9.2	6.7	7.3	7.3	10.2	2.0	8.6	3.9
265	10.4	6.6	8.1	5.9	13.4	1.7	11.9	1.6

hydroxyls. These observations suggest that methanol thermal decomposition involves additional dissimilar reaction routes on γ-Al_2O_3 than that of 30PTA/C500, boosting the formation of surface formates and desorption of HCOOH on γ-Al_2O_3. Overall, it is apparent that γ-Al_2O_3 facilitates both methanol dehydration and dehydrogenation, leading to formate/formic acid and CO formation, whereas PTA modification decreases surface area, enhances Brønsted acidity, and suppresses secondary oxidation pathways.

3.2. Catalytic Activity Experiments

To understand the effect of temperature on CO_2 conversion and product yield, CZA+γ-Al_2O_3 and CZA+30PTA/C500 catalyst (i.e., CZA+acid catalyst) mixtures are compared in one-step CO_2 to DME reaction at 215−265 °C, 3 MPa, H_2/CO_2 = 3, and CZA/acid catalyst mass ratios of 1/1−1/3. In the catalytic performance experiments using γ-Al_2O_3 as the acid catalyst, increasing temperature increases CO_2 conversion from ∼19 to ∼22% in both catalyst bed compositions (Figure 7a). This indicates that CO_2 is converted primarily via the endothermic RWGS reaction on the CZA catalyst, whose amount remains unchanged in this study. The weak response of CO_2 consumption to temperature change can be attributed to the combination of enhanced kinetics and the counteracting effects of CO and H_2O, which are consumed by reaction 2 and produced by reaction 3, respectively. DME yield increases from 2.0 to 8.2% upon changing the temperature from 215 to 265 °C. The negative effect of H_2O on the Lewis acid sites of the γ-Al_2O_3 catalyst due to competitive adsorption with methanol has been reported in previous studies.[27] Facilitating H_2O desorption from these sites by elevating the temperature improves DME formation.[81] Figure 7b also shows that DME yield is maximized at 8.3% at 255 °C, above which the thermodynamic limit is evident, with a slight decrease to 8.2% at 265 °C.

Considering the positive effect of surface acidity on the extent of reaction 3, incorporation of PTA to γ-Al_2O_3 is investigated to enhance the surface Brønsted acidity and improve resistance against deactivation via H_2O adsorption.[38] This hypothesis is examined by studying the CZA+30PTA/C500 catalyst mixture under conditions identical to those used to test the benchmark CZA+γ-Al_2O_3 system. The evolution of CO_2 conversion with temperature on CZA+30PTA/C500 differs slightly from that of the CZA+γ-Al_2O_3 benchmark (Figures 7a and 8a). The response of CO_2 conversion to temperature in the 215−235 °C range is more remarkable for CZA+30PTA/C500, where CO_2 conversion increases from 19% to 22% and from 17% to 23% at CZA+30PTA/C500 mass ratios of 1/1 and 1/3, respectively. At higher temperatures (245−265 °C), the dependence on catalyst composition fades out due to the onset of thermodynamic restrictions (Figure 8a). The impact of incorporating PTA into the acid catalyst is more evident in DME formation (Figure 8b). At the lowest temperature (215 °C), DME yield is 8.6%, which exceeds the value (2%) obtained on the benchmark γ-Al_2O_3 catalyst at CZA/acid catalyst ratio of 1/3. DME production on the 30PTA/C500 catalyst is further promoted by increasing temperature and maximized at ∼ 12% in the 235−245 °C range, where the DME yield on γ-Al_2O_3 is 7% (Figures 7b and 8b). After reaching 93% of its theoretical limit at 245 °C, the DME yield decreases at higher temperatures due to thermodynamic constraints on CO_2 conversion (Figure 8). The possibility of DME conversion to other hydrocarbons because of increased acidic strength is ruled out, since none of these products are detected by GC analysis. Moreover, the closure of the atomic carbon balance to <5% in each experiment (SI Section 1) ensures that neither carbon-containing compounds other than DME and MeOH, nor coke are generated to a significant extent.

https://doi.org/10.1021/acssuschemeng.5c13468
ACS Sustainable Chem. Eng. 2026, 14, 5650−5663

To provide useful insight into the trends in Figures 7 and 8, the yields of CO and MeOH are reported in Table 2. These results clearly show that CO formation increases with increasing temperature, regardless of catalyst type or composition. This finding is likely related to the increased extents of endothermic RWGS and the reverse of reaction 2, the latter of which is supported by the decreasing MeOH yields at elevated temperatures. Nevertheless, the response of Y_{MeOH} to temperature change is not as distinct as that of Y_{CO} due to the interplay between the reverse of reactions 2 and 3, which thermodynamically leads to the consumption and production of MeOH, respectively, at increased temperatures.

Comparative Y_{MeOH} values obtained in the presence of γ-Al_2O_3 and 30PTA/C500 catalysts provide solid evidence for the impacts of catalyst acidity on the extent of reaction 3. Presence of the Brønsted acid sites on the CZA+30PTA/C500 catalyst (see Section 3.1) leads to a significant leap in MeOH consumption and DME formation (Table 2 and Figures 7b and 8b). The difference between the performances of the acid catalysts is more evident at $T \leq 245$ °C where the adverse effects of the unwanted H_2O adsorption to the Lewis acid sites of the γ-Al_2O_3 are more severe. Along these lines, the strategy of minimizing H_2O adsorption by introducing Brønsted acidity appears useful for DME synthesis from CO_2 at low temperatures. The simultaneous decrease in the yields of DME and MeOH at $T \geq 245$ °C points out the fact that reaction 2 is reversed to a greater extent than DME to MeOH conversion *via* the reverse of Reaction (3).

Table 2 provides insight into the effects of catalyst compositions on performance. Increasing the CZA/acid catalyst mass ratio from 1/1 to 1/3 decreases the yields of CO and MeOH, the latter of which is consumed due to the increased availability of acid sites and the resulting longer contact with the reactive mixture, whose feed flow rate is unchanged in the experiments (Section 2.3). This finding is consistent with higher DME yields at higher amounts of acid catalyst (Figures 7b and 8b). Increased MeOH consumption via reaction 3 thermodynamically promotes CO hydrogenation, thereby reducing CO yields (Table 2). The results also reveal that, despite the longer interaction time of the reactive flow due to the increased amount of acid catalyst, the magnitude of change in DME and MeOH yields as a function of catalyst composition is weaker for the CZA+30PTA/C500 catalyst mixture. In other words, DME can be synthesized with less acid catalyst inventory, which is particularly important when considering the complex hydrodynamics and heat transfer requirements of larger production scales. To highlight the effect of increasing acid catalyst loading, performance is also evaluated in terms of catalyst productivity, defined as the mass of DME produced per unit mass of catalyst (CZA + acid catalyst) per unit time. This metric, calculated for all combinations of catalyst type, catalyst composition, and reaction temperature, is presented in Figure 9. The results clearly reveal higher productivities in favor of using a smaller mass of acid catalyst (i.e., mass ratio = 1/1) except for CZA/γ-Al_2O_3 = 1/3 at 215−235 °C where the additional use of the γ-Al_2O_3 catalyst justifies the increase in DME production. The maximum productivity of 6.9×10^{-3} kg_{DME} kg_{cat}^{-1} h^{-1} and approach to equilibrium (93% of the theoretical DME yield) are found at 245 °C and CZA/30PTA/C500 = 1/1. At these conditions, the CZA+γ-Al_2O_3 system delivers 2.9×10^{-3} kg_{DME} kg_{cat}^{-1} h^{-1} of DME productivity and can be maximized only to 3.8×10^{-3} kg_{DME} kg_{cat}^{-1} h^{-1} at 265 °C. These findings clearly show that the use of 30PTA/C500 catalyst is more suited to CO_2-to-DME conversion at low temperatures (< 245 °C), where reactor intensification strategies, such as in situ H_2O adsorption, can further improve catalyst productivity.[23−26]

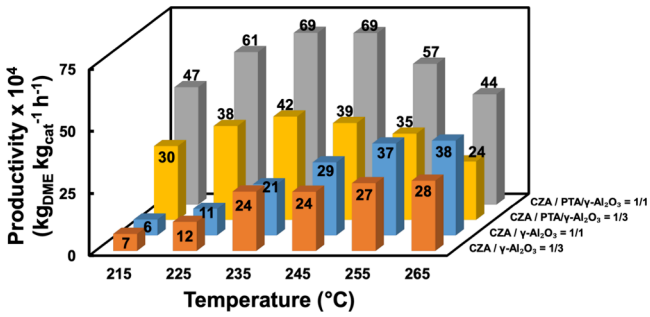

Figure 9. Catalyst productivity (kg_{DME} $kg_{CZA+acid\_catalyst}^{-1}$ h^{-1}) as functions of reaction temperature (215−265 °C), catalyst type (CZA +30PTA/C500 and CZA+γ-Al_2O_3), and catalyst composition (CZA/acid catalyst mass ratios = 1/1 and 1/3).

The catalyst type, composition, and the conditions leading to peak productivity are investigated in the 1.5−3 MPa range to understand the effect of pressure on reaction performance. The results presented in Figure 10 show that increasing the pressure improves CO_2 conversion and DME yield, from 16.8 to 21.4% and from 4.1 to 10.3%, respectively. CO_2 and DME are involved in equimolar reactions 1 and 3 that are individually insensitive to pressure variation. However, these reactions are affected by kinetic and thermodynamic promotion of CO hydrogenation at high pressures, which promote CO consumption and MeOH formation through the RWGS and MeOH dehydration reactions, respectively.[4] Even though the trend in Figure 10 continues at pressures > 3 MPa, this value is reported as optimal when the balance between the fixed and operating cost of increasing pressure and the improvement in performance metrics are considered.[82]

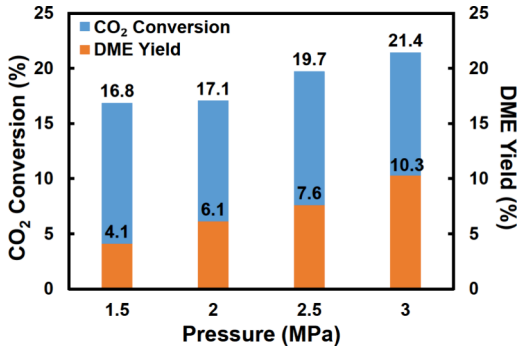

Figure 10. Effect of pressure on CO_2 conversion and DME yield obtained at 245 °C on the CZA+30PTA/C500 catalyst mixture at CZA/(30PTA/C500) mass ratio = 1/1.

3.3. Catalytic Stability Experiments

The CZA+30PTA/C500 catalyst mixture is tested for stability in a 72 h TOS experiment conducted under peak productivity conditions. Initially, the catalyst mixture gives 21.8% CO_2 conversion and yields 10.2% DME, 7.5% MeOH, and 6.1% CO (Figure 11). At the end of 72 h, CO_2 conversion and DME yield decrease by 8 and 13%, respectively, and MeOH yield declines by 1%. The initial DME selectivity ($=2F_{DME} \times 100/(2F_{DME} + F_{MeOH} + F_{CO})$), 42.8%, is found to diminish by

https://doi.org/10.1021/acssuschemeng.5c13468
ACS Sustainable Chem. Eng. 2026, 14, 5650−5663

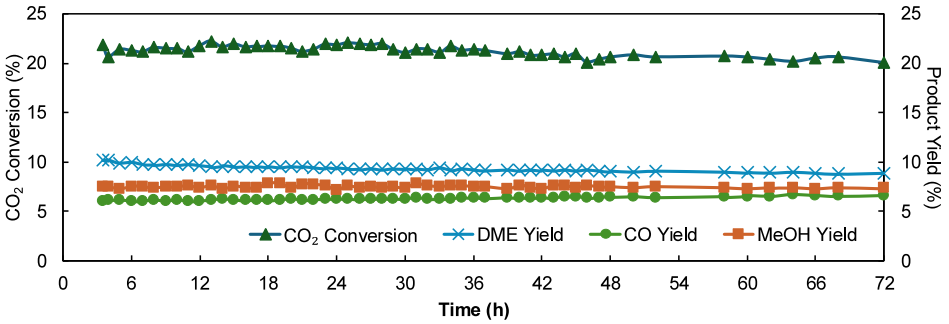

Figure 11. 72 h TOS stability testing of the CZA+30PTA/C500 catalyst mixture at CZA/(30PTA/C500) mass ratio = 1/1, 245 °C, and 3 MPa.

~10%. In contrast, CO yield increases by ~ 8% (Figure 11). The atomic carbon balance is closed to an average of 2% in the duration of the TOS experiment. This data rules out a significant extent of coke formation in the current catalyst system and operating conditions. Decreasing MeOH and increasing CO yields in Figure 11 are correlated with the reversal of reaction 2, which is presumably caused by the decrease in the extent of MeOH dehydration reaction, possibly due to H_2O accumulation in the reactive mixture, and, most likely, its competitive H_2O adsorption to the Lewis acid sites of the 30PTA/C500 catalyst.[83] The increase in CO yield may also explain the decrease in CO_2 conversion via the water−gas shift reaction (i.e., the reverse of reaction 1). The results in Figure 11 also show that the deactivation rate decreases over time. The changes in CO_2 conversion and DME yield do not exceed 3% in the 48−72 h period. This suggests that the possible adverse effects of H_2O affect performance at earlier stages and that the catalysts eventually approach a steady state.

The TOS stability performance of the CZA+30PTA/C500 system is compared with that of systems involving zeolites as the acid function. It is reported that 100 h of CO_2 hydrogenation at 240 °C, 2.8 MPa, 1525 NL kg_{cat}^{-1} h^{-1}, and H_2/CO_2 = 3/1 on the Cu-ZnO/H-ZSM-5 catalyst mixture results in ~ 16% and 33% decreases in CO_2 conversion and DME yield, respectively.[32] Long-term testing the same reaction at 260 °C, 3 MPa, 8800 NL kg_{cat}^{-1} h^{-1} and $H_2/CO_2/N_2$ = 9/3/1 on CZZ/Zeolite (Sil-1, MFI, Zeolite Y, FER, BEA, MOR) mixtures decreases CO_2 conversion and DME selectivity in the ranges of ~13−38 and ~17−24%, respectively, as of 72 h from the onset of the experiments.[16] Considering the literature data reported at operating conditions similar to those in the present work (Table S6), the CZA+30PTA/C500 catalyst appears to exhibit superior stability compared to zeolite-based catalysts.

4. CONCLUSIONS

This study establishes a structure−functionality relationship between nature and the relative extent of surface acidic sites, and the catalytic performance in one-step CO_2-to-DME conversion using bifunctional CZA+PTA/γ-Al_2O_3 catalysts. Brønsted acidity is significantly enhanced by PTA incorporation, and the optimal composition, 30 wt.% PTA loading calcined at 500 °C, exhibits the highest Brønsted/Lewis acid site ratio and total acid site density, as confirmed by NH_3-TPD, and pyridine adsorption via in situ FTIR analyses. Structural characterization reveals that under these conditions, PTA remains in a well-dispersed or amorphous state, whereas higher temperatures cause the formation of WO_3 crystallites and a corresponding decrease in Brønsted acidity. XPS and TPR analyses show that tungsten predominantly exists in the stable W^{6+} oxidation state, with no significant reduction to W^{5+}, indicating the catalyst's hydrothermal stability. In situ FTIR studies demonstrate that methanol dehydration proceeds via a direct DME-forming route, without the formation of formate intermediates, suggesting a Brønsted acid-mediated associative, direct concerted mechanism. Moreover, methanol-TPD analyses show that methanol either desorbs and converts into DME on the PTA-modified catalyst, while methanol dehydrogenation and byproduct (formic acid, CO) formation are strongly suppressed, indicating a direct DME-formation pathway on Brønsted acid-enriched surfaces. Physical mixing of the optimized 30PTA/C500 catalyst with conventional CZA at equal masses achieves a maximum DME productivity of 6.9 × 10^{-3} kg_{DME} kg_{cat}^{-1} h^{-1} at 245 °C and 3 MPa, significantly outperforming the benchmark case involving γ-Al_2O_3 as the acid catalyst. Furthermore, a limited 72 h TOS activity loss of ~8%, which decreased to <3% in the 48−72 h time span, highlights strong resistance to steam-induced deactivation. These findings demonstrate that tuning surface acidity and preserving structural integrity are key strategies for enhancing activity, selectivity, and long-term stability in the valorization of CO_2 to DME.

■ ASSOCIATED CONTENT

Supporting Information

The Supporting Information is available free of charge at https://pubs.acs.org/doi/10.1021/acssuschemeng.5c13468.

Calculation of the atomic carbon balances; interpretation and calculation of CO_2 conversion via GC analysis; activity tests for benchmarking the synthesized CZA catalyst; and description of the techniques used in characterizing the PTA/γ-Al_2O_3 catalyst (PDF)

■ AUTHOR INFORMATION

Corresponding Author

Ahmet K. Avci − *Department of Chemical Engineering, Bogazici University, Istanbul 34342, Turkey;* orcid.org/0000-0003-4082-7005; Email: avciahme@bogazici.edu.tr

Authors

Mert Ozden − *Department of Chemical Engineering, Bogazici University, Istanbul 34342, Turkey;* orcid.org/0000-0003-0350-1313

N. Semih Altinsoy − *Department of Chemical Engineering, Bogazici University, Istanbul 34342, Turkey;* orcid.org/0000-0002-6262-3938

Ahsan Jalal − *Department of Chemistry, Bilkent University, Ankara 06800, Turkey;* Present Address: Department of

https://doi.org/10.1021/acssuschemeng.5c13468
ACS Sustainable Chem. Eng. 2026, 14, 5650−5663

Chemical Engineering, GIK Institute of Engineering Sciences and Technology, 23640, Khyber Pakhtunkhwa, Pakistan

Ayse Dilay Erdali − *Department of Chemistry, Bilkent University, Ankara 06800, Turkey;* orcid.org/0000-0002-5065-1317

Orhan Ozcan − *Department of Chemical Engineering, Kocaeli University, Kocaeli 41001, Turkey*

Ayse Nilgun Akin − *Department of Chemical Engineering, Kocaeli University, Kocaeli 41001, Turkey*

Emrah Ozensoy − *Department of Chemistry and UNAM-National Nanotechnology Center, Bilkent University, Ankara 06800, Turkey;* orcid.org/0000-0003-4352-3824

Complete contact information is available at: https://pubs.acs.org/10.1021/acssuschemeng.5c13468

Author Contributions

†M.O. and N.S.A. contributed equally to this work.

Notes

The authors declare no competing financial interest.

■ ACKNOWLEDGMENTS

Financial support is provided by TUBITAK [grant number: 120M412] and Bogazici University Research Fund [grant number: 20683].

■ REFERENCES

(1) Centi, G.; Quadrelli, E. A.; Perathoner, S. Catalysis for CO_2 conversion: a key technology for rapid introduction of renewable energy in the value chain of chemical industries. *Energy Environ. Sci.* **2013**, *6* (6), 1711−1731.

(2) Omodolor, I. S.; Otor, H. O.; Andonegui, J. A.; Allen, B. J.; Alba-Rubio, A. C. Dual-function materials for CO_2 capture and conversion: a review. *Ind. Eng. Chem. Res.* **2020**, *59* (40), 17612−17631.

(3) Mondal, U.; Yadav, G. D. Perspective of dimethyl ether as fuel: Part I. Catalysis. *J. CO2 Util.* **2019**, *32*, 299−320.

(4) Ateka, A.; Rodriguez-Vega, P.; Ereña, J.; Aguayo, A. T.; Bilbao, J. A review on the valorization of CO_2. Focusing on the thermodynamics and catalyst design studies of the direct synthesis of dimethyl ether. *Fuel Process. Technol.* **2022**, *233*, No. 107310.

(5) Semelsberger, T. A.; Borup, R. L.; Greene, H. L. Dimethyl ether (DME) as an alternative fuel. *J. Power Sources* **2006**, *156* (2), 497−511.

(6) Peinado, C.; Liuzzi, D.; Sluijter, S. N.; Skorikova, G.; Boon, J.; Guffanti, S.; Groppi, G.; Rojas, S. Review and perspective: Next generation DME synthesis technologies for the energy transition. *Chem. Eng. J.* **2024**, *479*, No. 147494.

(7) Mondal, U.; Yadav, G. D. Perspective of dimethyl ether as fuel: Part II- analysis of reactor systems and industrial processes. *J. CO2 Util.* **2019**, *32*, 321−338.

(8) Azizi, Z.; Rezaeimanesh, M.; Tohidian, T.; Rahimpour, M. R. Dimethyl ether: A review of technologies and production challenges. *Chem. Eng. Process.: Process Intensif.* **2014**, *82*, 150−172.

(9) Saravanan, K.; Ham, H.; Tsubaki, N.; Bae, J. W. Recent progress for direct synthesis of dimethyl ether from syngas on the heterogeneous bifunctional hybrid catalysts. *Appl. Catal., B* **2017**, *217*, 494−522.

(10) Venvik, H. J.; Yang, J. Catalysis in microstructured reactors: Short review on small-scale syngas production and further conversion into methanol, DME and Fischer−Tropsch products. *Catal. Today* **2017**, *285*, 135−146.

(11) Rothenberg, G. A realistic look at CO_2 emissions, climate change and the role of sustainable chemistry. *Sustain. Chem. Clim. Action* **2023**, *2*, No. 100012.

(12) Lee, B.; Winter, L. R.; Lee, H.; Lim, D.; Lim, H.; Elimelech, M. Pathways to a green ammonia future. *ACS Energy Lett.* **2022**, *7* (9), 3032−3038.

(13) Catizzone, E.; Bonura, G.; Migliori, M.; Frusteri, F.; Giordano, G. CO_2 recycling to dimethyl ether: State-of-the-art and perspectives. *Molecules* **2018**, *23* (1), 31.

(14) Temvuttirojn, C.; Chuasomboon, N.; Numpilai, T.; Faungnawakij, K.; Chareonpanich, M.; Limtrakul, J.; Witoon, T. Development of SO_4^{2-}−ZrO_2 acid catalysts admixed with a CuO-ZnO-ZrO_2 catalyst for CO_2 hydrogenation to dimethyl ether. *Fuel* **2019**, *241*, 695−703.

(15) Bonura, G.; Cannilla, C.; Frusteri, L.; Mezzapica, A.; Frusteri, F. DME production by CO_2 hydrogenation: Key factors affecting the behaviour of CuZnZr/ferrierite catalysts. *Catal. Today* **2017**, *281*, 337−344.

(16) Bonura, G.; Cannilla, C.; Frusteri, L.; Catizzone, E.; Todaro, S.; Migliori, M.; Giordano, G.; Frusteri, F. Interaction effects between CuO-ZnO-ZrO_2 methanol phase and zeolite surface affecting stability of hybrid systems during one-step CO_2 hydrogenation to DME. *Catal. Today* **2020**, *345*, 175−182.

(17) Bonura, G.; Migliori, M.; Frusteri, L.; Cannilla, C.; Catizzone, E.; Giordano, G.; Frusteri, F. Acidity control of zeolite functionality on activity and stability of hybrid catalysts during DME production via CO_2 hydrogenation. *J. CO2 Util.* **2018**, *24*, 398−406.

(18) Ateka, A.; Rodriguez-Vega, P.; Cordero-Lanzac, T.; Bilbao, J.; Aguayo, A. T. Model validation of a packed bed LTA membrane reactor for the direct synthesis of DME from CO/CO_2. *Chem. Eng. J.* **2021**, *408*, No. 127356.

(19) Rodriguez-Vega, P.; Ateka, A.; Kumakiri, I.; Vicente, H.; Ereña, J.; Aguayo, A. T.; Bilbao, J. Experimental implementation of a catalytic membrane reactor for the direct synthesis of DME from H_2+CO/CO_2. *Chem. Eng. Sci.* **2021**, *234*, No. 116396.

(20) Koybasi, H. H.; Hatipoglu, C.; Avci, A. K. Sustainable DME synthesis from CO_2−rich syngas in a membrane assisted reactor−microchannel heat exchanger system. *J. CO2 Util.* **2021**, *52*, No. 101660.

(21) Koybasi, H. H.; Avci, A. K. Modeling of a membrane integrated catalytic microreactor for efficient DME production from syngas with CO_2. *Catal. Today* **2022**, *383*, 133−145.

(22) Koybasi, H. H.; Avci, A. K. Numerical analysis of CO_2-to-DME conversion in a membrane microchannel reactor. *Ind. Eng. Chem. Res.* **2022**, *61*, 10846−10859.

(23) Ozden, M.; Altinsoy, N. S.; Avci, A. K. Comprehensive parametric assessment of steam-adsorption intensified hydrogenation of CO_2 to DME. *Int. J. Hydrog. Energy* **2025**, *172*, No. 151320.

(24) Altinsoy, N. S.; Avci, A. K. Sorption enhanced DME synthesis by one-step CO_2 hydrogenation. *Chem. Eng. Process.: Process Intensif.* **2024**, *203*, No. 109874.

(25) van Kampen, J.; Boon, J.; Vente, J.; van Sint Annaland, M. Sorption enhanced dimethyl ether synthesis for high efficiency carbon conversion modelling and cycle design. *J. CO2 Util.* **2020**, *37*, 295−308.

(26) van Kampen, J.; Booneveld, S.; Boon, J.; Vente, J.; van Sint Annaland, M. Sint Annaland, Experimental validation of pressure swing regeneration for faster cycling in sorption enhanced dimethyl ether synthesis. *Chem. Commun.* **2020**, *56* (88), 13540−13542.

(27) Xu, M.; Lunsford, J. H.; Goodman, D. W.; Bhattacharyya, A. Synthesis of dimethyl ether (DME) from methanol over solid-acid catalysts. *Appl. Catal. A: Gen.* **1997**, *149* (2), 289−301.

(28) Said, A.E.-A.A.; Abd El-Wahab, M. M. M.; Abdelhak, M. M. The role of Brønsted acid site strength on the catalytic performance of phosphotungstic acid supported on nano γ-alumina catalysts for the dehydration of ethanol to diethyl ether. *React. Kinet. Mech. Catal.* **2017**, *122* (1), 433−449.

(29) Akarmazyan, S. S.; Panagiotopoulou, P.; Kambolis, A.; Papadopoulou, C.; Kondarides, D. I. Methanol dehydration to dimethylether over Al_2O_3 catalysts. *Appl. Catal., B* **2014**, *145*, 136−148.

(30) Fan, X.; Jin, B.; Ren, S.; Li, S.; Yu, M.; Liang, X. Roles of interaction between components in CZZA/HZSM-5 catalyst for dimethyl ether synthesis via CO_2 hydrogenation. *AIChE J.* **2021**, *67* (11), No. e17353.
(31) Krim, K.; Sachse, A.; Le Valant, A.; Pouilloux, Y.; Hocine, S. One step dimethyl ether (DME) synthesis from CO_2 hydrogenation over hybrid catalysts containing $Cu/ZnO/Al_2O_3$ and nano-sized hollow ZSM-5 zeolites. *Catal. Lett.* **2023**, *153* (1), 83−94.
(32) Ren, S.; Shoemaker, W. R.; Wang, X.; Shang, Z.; Klinghoffer, N.; Li, S.; Yu, M.; He, X.; White, T. A.; Liang, X. Highly active and selective Cu-ZnO based catalyst for methanol and dimethyl ether synthesis via CO_2 hydrogenation. *Fuel* **2019**, *239*, 1125−1133.
(33) Naik, S. P.; Ryu, T.; Bui, V.; Miller, J. D.; Drinnan, N. B.; Zmierczak, W. Synthesis of DME from CO_2/H_2 gas mixture. *Chem. Eng. J.* **2011**, *167* (1), 362−368.
(34) Catizzone, E.; Daele, S. V.; Bianco, M.; Di Michele, A.; Aloise, A.; Migliori, M.; Valtchev, V.; Giordano, G. Catalytic application of ferrierite nanocrystals in vapour-phase dehydration of methanol to dimethyl ether. *Appl. Catal., B* **2019**, *243*, 273−282.
(35) Catizzone, E.; Migliori, M.; Purita, A.; Giordano, G. Ferrierite vs. γ-Al_2O_3: The superiority of zeolites in terms of water-resistance in vapour-phase dehydration of methanol to dimethyl ether. *J. Energy Chem.* **2019**, *30*, 162−169.
(36) Baek, S.-C.; Lee, Y.-J.; Jun, K.-W.; Hong, S. B. Influence of catalytic functionalities of zeolites on product selectivities in methanol conversion. *Energy Fuel.* **2009**, *23* (2), 593−598.
(37) García-Trenco, A.; Vidal-Moya, A.; Martínez, A. Study of the interaction between components in hybrid CuZnAl/HZSM-5 catalysts and its impact in the syngas-to-DME reaction. *Catal. Today* **2012**, *179* (1), 43−51.
(38) Peinado, C.; Liuzzi, D.; Ladera-Gallardo, R. M.; Retuerto, M.; Ojeda, M.; Peña, M. A.; Rojas, S. Effects of support and reaction pressure for the synthesis of dimethyl ether over heteropolyacid catalysts. *Sci. Rep.* **2020**, *10* (1), 8551.
(39) Şeker, B.; Dizaji, A. K.; Balci, V.; Uzun, A. MCM-41-supported tungstophosphoric acid as an acid function for dimethyl ether synthesis from CO_2 hydrogenation. *Renew. Energy* **2021**, *171*, 47−57.
(40) Baracchini, G.; Klumpp, M.; Arnold, P.; Dittmeyer, R. Direct synthesis of dimethyl ether: A simulation study on the influence of the catalyst configuration. *Chem. Eng. J.* **2020**, *396*, No. 125155.
(41) Bonura, G.; Cordaro, M.; Cannilla, C.; Mezzapica, A.; Spadaro, L.; Arena, F.; Frusteri, F. Catalytic behaviour of a bifunctional system for the one step synthesis of DME by CO_2 hydrogenation. *Catal. Today* **2014**, *228*, 51−57.
(42) Onsan, Z. I., Avci, A. K., Reactor design for fuel processing, in: Shekhawat, D., Spivey, J. J., Berry, D. A. (Eds.), *Fuel Cells: Technologies for Fuel Processing*; Elsevier Science, Amsterdam, 2011; pp 451−516. .
(43) Kubas, D.; Beck, J. M.; Kasisari, E.; Schätzler, T.; Becherer, A.; Fischer, A.; Krossing, I. From CO_2 to DME: Enhancement through heteropoly acids from a catalyst screening and stability study. *ACS Omega* **2023**, *8* (17), 15203−15216.
(44) Wesner, A.; Herrmann, N.; Prawitt, L.; Ortmann, A.; Albert, J.; Poller, M. J. Study of supported heteropolyacid catalysts for one-step DME synthesis from CO_2 and H_2. *RSC Adv.* **2025**, *15* (1), 38−47.
(45) Matkovic, S. R.; Bosco, M.; Collins, S. E.; Briand, L. E. Tailored Brønsted and Lewis surface acid sites of the phosphotungstic Wells Dawson heteropoly-acid. *Appl. Surf. Sci.* **2019**, *495*, No. 143565.
(46) Zhu, S.; Gao, X.; Dong, F.; Zhu, Y.; Zheng, H.; Li, Y. Design of a highly active silver-exchanged phosphotungstic acid catalyst for glycerol esterification with acetic acid. *J. Catal.* **2013**, *306*, 155−163.
(47) Busca, G. Spectroscopic characterization of the acid properties of metal oxide catalysts. *Catal. Today* **1998**, *41* (1), 191−206.
(48) Zaki, M. I.; Hasan, M. A.; Al-Sagheer, F. A.; Pasupulety, L. In situ FTIR spectra of pyridine adsorbed on SiO_2−Al_2O_3, TiO_2, ZrO_2 and CeO_2: general considerations for the identification of acid sites on surfaces of finely divided metal oxides. *Colloids Surf. A: Physicochem. Eng. Asp* **2001**, *190* (3), 261−274.
(49) Morterra, C.; Chiorino, A.; Ghiotti, G.; Garrone, E. Surface acidity of η-alumina. Part 1.—Pyridine chemisorption at room temperature. *J. Chem. Soc. Faraday Trans. 1: Phys. Chem. Condensed Phases* **1979**, *75* (0), 271−288.
(50) Lundie, D. T.; McInroy, A. R.; Marshall, R.; Winfield, J. M.; Jones, P.; Dudman, C. C.; Parker, S. F.; Mitchell, C.; Lennon, D. Improved description of the surface acidity of η-Alumina. *J. Phys. Chem. B* **2005**, *109* (23), 11592−11601.
(51) Ma, T.; Ding, J.; Shao, R.; Xu, W.; Yun, Z. Dehydration of glycerol to acrolein over Wells−Dawson and Keggin type phosphotungstic acids supported on MCM-41 catalysts. *Chem. Eng. J.* **2017**, *316*, 797−806.
(52) Atia, H.; Armbruster, U.; Martin, A. Dehydration of glycerol in gas phase using heteropolyacid catalysts as active compounds. *J. Catal.* **2008**, *258* (1), 71−82.
(53) Emeis, C. A. Determination of integrated molar extinction coefficients for infrared absorption bands of pyridine adsorbed on solid acid catalysts. *J. Catal.* **1993**, *141* (2), 347−354.
(54) Wang, X.; Lv, T.; Wu, M.; Sui, J.; Liu, Q.; Liu, H.; Huang, J.; Jia, L. Aluminum doped solid acid with suitable ratio of Brønsted and Lewis acid sites synthesized by electric-flocculation of phosphotungstic acid via hydrothermal treatment for producing 5-hydroxymethylfurfural from glucose. *Appl. Catal. A: Gen.* **2019**, *574*, 87−96.
(55) Parida, K. M.; Mallick, S. Phosphotungstic acid promoted zirconia−alumina mixed oxides: A stable and reusable catalysts for epoxidation of trans-stilbene. *Catal. Commun.* **2009**, *11* (1), 51−57.
(56) Gao, J.; Wei, Y.; Wang, X.; Yang, W. Tungstophosphoric heteropolyacid supported onto neutral alumina: characterization and synthesis of acetals and ketals. *Rare Met.* **2007**, *26* (2), 152−157.
(57) Chan, S. S.; Wachs, I. E.; Murrell, L. L.; Dispenziere, N. C. Laser Raman characterization of tungsten oxide supported on alumina: Influence of calcination temperatures. *J. Catal.* **1985**, *92* (1), 1−10.
(58) Ruan, H. D.; Frost, R. L.; Kloprogge, J. T. Comparison of Raman spectra in characterizing gibbsite, bayerite, diaspore and boehmite. *J. Raman Spectrosc.* **2001**, *32* (9), 745−750.
(59) Wachs, I. E.; Kim, T.; Ross, E. I. Catalysis science of the solid acidity of model supported tungsten oxide catalysts. *Catal. Today* **2006**, *116* (2), 162−168.
(60) Highfield, J. G.; Moffat, J. B. Characterization of 12-tungstophosphoric acid and related salts using photoacoustic spectroscopy in the infrared region: I. Thermal stability and interactions with ammonia. *J. Catal.* **1984**, *88* (1), 177−187.
(61) Ilbeygi, H.; Kim, I. Y.; Kim, M. G.; Cha, W.; Kumar, P. S. M.; Park, D.-H.; Vinu, A. Highly crystalline mesoporous phosphotungstic acid: a high-performance electrode material for energy-storage applications. *Angew. Chem., Int. Ed.* **2019**, *58* (32), 10849−10854.
(62) Moulder, J. F., Chastain, J.*Handbook of X-ray Photoelectron Spectroscopy: A Reference Book of Standard Spectra for Identification and Interpretation of XPS Data*; Physical Electronics Division, Perkin-Elmer Corporation1992.
(63) Li, H.; Abdelgaid, M.; Paudel, J. R.; Holzapfel, N. P.; Augustyn, V.; McKone, J. R.; Mpourmpakis, G.; Crumlin, E. J. Operando unveiling of hydrogen spillover mechanisms on tungsten oxide surfaces. *J. Am. Chem. Soc.* **2025**, *147* (8), 6472−6479.
(64) Mizuno, N.; Watanabe, T.; Misono, M. Catalysis by hetropoly compounds. 16. Catalytic oxidation and isotopic exchange of hydrogen over 12-molybdophosphoric acid. *J. Phys. Chem.* **1990**, *94* (2), 890−894.
(65) Hodnett, B. K.; Moffat, J. B. Application of temperature-programmed desorption to the study of heteropoly compounds: Desorption of water and pyridine. *J. Catal.* **1984**, *88* (2), 253−263.
(66) Braaten, O.; Kjekshus, A.; Kvande, H. The possible reduction of alumina to aluminum using hydrogen. *JOM* **2000**, *52* (2), 47−53.
(67) Okuhara, T., Mizuno, N., Misono, M., Catalytic Chemistry of Heteropoly Compounds, in: Eley, D. D., Haag, W. O., Gates, B. (Eds.), *Adv. Catal.*; Academic Press1996; pp 113−252. .
(68) Spivey, J. J. Review: Dehydration catalysts for the methanol/dimethyl ether reaction. *Chem. Eng. Commun.* **1991**, *110* (1), 123−142.

https://doi.org/10.1021/acssuschemeng.5c13468
ACS Sustainable Chem. Eng. 2026, 14, 5650−5663

(69) Schiffino, R. S.; Merrill, R. P. A mechanistic study of the methanol dehydration reaction on.gamma.-alumina catalyst. *J. Phys. Chem.* **1993**, *97* (24), 6425−6435.
(70) Carr, R. T.; Neurock, M.; Iglesia, E. Catalytic consequences of acid strength in the conversion of methanol to dimethyl ether. *J. Catal.* **2011**, *278* (1), 78−93.
(71) Moses, P. G.; Nørskov, J. K. Methanol to dimethyl ether over ZSM-22: a periodic density functional theory study. *ACS Catal.* **2013**, *3* (4), 735−745.
(72) Khaleel, A.; Ahmed, M.a.; Sowaid, S. B. Ti-doped γ-Al_2O_3 versus ZSM5 zeolites for methanol to dimethyl ether conversion: In-situ DRIFTS investigation of surface interactions and reaction mechanism. *Colloids Surf. A: Physicochem. Eng. Asp.* **2019**, *571*, 174−181.
(73) Matyshak, V. A.; Berezina, L. A.; Sil'chenkova, O. N.; Tret'yakov, V. F.; Lin, G. I.; Rozovskii, A. Y. Properties of surface compounds in methanol conversion on γ-Al_2O_3: Data of in situ IR spectroscopy. *Kinet. Catal.* **2009**, *50* (1), 111−121.
(74) Busca, G. Infrared studies of the reactive adsorption of organic molecules over metal oxides and of the mechanisms of their heterogeneously-catalyzed oxidation. *Catal. Today* **1996**, *27* (3), 457−496.
(75) Bondarenko, G. N.; Volnina, E. A.; Kipnis, M. A.; Rodionov, A. S.; Samokhin, P. V.; Lin, G. I. Surface reactions of dimethyl ether on γ-Al_2O_3. *Russ. J. Phys. Chem. A* **2016**, *90* (2), 458−465.
(76) Al-Abadleh, H. A.; Grassian, V. H. FT-IR study of water adsorption on aluminum oxide surfaces. *Langmuir* **2003**, *19* (2), 341−347.
(77) Busca, G.; Lamotte, J.; Lavalley, J. C.; Lorenzelli, V. FT-IR study of the adsorption and transformation of formaldehyde on oxide surfaces. *J. Am. Chem. Soc.* **1987**, *109* (17), 5197−5202.
(78) Lotfollahzade Moghaddam, A.; Hazlett, M. J. Methanol dehydration catalysts in direct and indirect dimethyl ether (DME) production and the beneficial role of DME in energy supply and environmental pollution. *J. Environ. Chem. Eng.* **2023**, *11* (3), No. 110307.
(79) Mota, N.; Millán Ordoñez, E.; Pawelec, B.; Fierro, J. L. G.; Navarro, R. M. Direct synthesis of dimethyl ether from CO2. *Recent advances in bifunctional/hybrid catalytic systems, Catalysts* **2021**, *11*, 411.
(80) Burcham, L. J.; Briand, L. E.; Wachs, I. E. Quantification of active sites for the determination of methanol oxidation turn-over frequencies using methanol chemisorption and in situ infrared techniques. 1. supported metal oxide catalysts. *Langmuir* **2001**, *17* (20), 6164−6174.
(81) Takeguchi, T.; Yanagisawa, K.-i.; Inui, T.; Inoue, M. Effect of the property of solid acid upon syngas-to-dimethyl ether conversion on the hybrid catalysts composed of Cu−Zn−Ga and solid acids. *Appl. Catal. A Gen.* **2000**, *192* (2), 201−209.
(82) Bonura, G.; Todaro, S.; Frusteri, L.; Majchrzak-Kucęba, I.; Wawrzyńczak, D.; Pászti, Z.; Tálas, E.; Tompos, A.; Ferenc, L.; Solt, H.; Cannilla, C.; Frusteri, F. Inside the reaction mechanism of direct CO_2 conversion to DME over zeolite-based hybrid catalysts. *Appl. Catal. B: Environ.* **2021**, *294*, No. 120255.
(83) Raoof, F.; Taghizadeh, M.; Eliassi, A.; Yaripour, F. Effects of temperature and feed composition on catalytic dehydration of methanol to dimethyl ether over γ-alumina. *Fuel* **2008**, *87* (13), 2967−2971.

https://doi.org/10.1021/acssuschemeng.5c13468
ACS Sustainable Chem. Eng. 2026, 14, 5650−5663